Research Article

Yingwu Zhou, Li Zhuang, Zhiheng Hu, Biao Hu*, Xiaoxu Huang, Shan Li, Menghuan Guo, and Zhongfeng Zhu

Perforated steel block of realizing large ductility under compression: Parametric study and stress-strain modeling

https://doi.org/10.1515/rams-2022-0026 received September 21, 2021; accepted January 31, 2022

Abstract: On one hand, the nature of linear elastic up to brittle rupture hinders the application of fiber-reinforced polymer (FRP) bars as reinforcement in the concrete member due to the displacement ductility demand of structures. On the other hand, FRP bars are equipped with many irreplaceable advantages as reinforcement in concrete structures. To resolve this contradiction, a possible solution is to use the so-called compression yield (CY) structural system and the ductility of a concrete beam incorporating a CY system comes from the compressive side rather than the tensile side. Thus, the development of material in the compressive side (CY material) with well-designed mechanical properties (strength, stiffness, and ductility) is a key challenge. In this study, the CY material is developed by perforating the mild steel block and then substantiated by the test results. Then,

experimentally calibrated finite element models are used to conduct systematic parametric studies, based on which parametric equations are proposed to predict the stiffness and ultimate strength of the CY material. Finally, theoretical constitutive models are developed to predict the stress–strain response of perforated steel block under compression and a reasonably acceptable agreement is reached between the model predictions and the test results.

Reviews on Advanced Materials Science 2022; 61: 221-237

Keywords: perforation, compression yield, stress–strain model

1 Introduction

During the service life of reinforced concrete (RC) structures, their structural performances are likely to be deteriorated by corrosive medium [1,2], especially those constructed in coastal environments decades ago. Thus, the durability problem of such kinds of structures needs special concern and coping strategy to reduce maintenance costs and mitigate structural failure risks [3-5]. Recently, fiber-reinforced polymer (FRP) has gained extensive attention due to its anti-corrosion nature and low maintenance cost and has been widely used in strengthening or retrofitting existing RC structures by plating or jacketing [6–8]. However, for new structures, using FRP bars to replace conventional steel bars as reinforcement in concrete structures remains a challenge due to the significantly reduced ductility caused by the linear elastic up to brittle rupture behavior of FRP bars. Naaman [9] summarized six methods to improve the ductility of concrete members reinforced by FRP bars, including providing confinement to concrete; placing prestressed FRP bars in layers with the well-designed prestress to reach a progressive failure; combining FRP bars with steel rebar to form the so-called hybrid reinforcing system; using unbonded FRP tendons; designing the FRP-concrete bonding interface to trigger bond failure at certain stress level; and optimizing the reinforcement ratio

Yingwu Zhou, Xiaoxu Huang, Menghuan Guo, Zhongfeng Zhu:
College of Civil and Transportation Engineering, Guangdong
Provincial Key Laboratory of Durability for Marine Civil Engineering,
Shenzhen University, Shenzhen, 518060, China; College of Civil and
Transportation Engineering, Key Laboratory for Resilient
Infrastructures of Coastal Cities (Shenzhen University), Ministry of
Education, Shenzhen, China

Li Zhuang, Zhiheng Hu: College of Civil and Transportation Engineering, Guangdong Provincial Key Laboratory of Durability for Marine Civil Engineering, Shenzhen University, Shenzhen, 518060, China

Shan Li: College of Civil and Transportation Engineering, School of Civil Engineering, Wuhan University, Wuhan, 430072, China

^{*} Corresponding author: Biao Hu, College of Civil and Transportation Engineering, Guangdong Provincial Key Laboratory of Durability for Marine Civil Engineering, Shenzhen University, Shenzhen, 518060, China; College of Civil and Transportation Engineering, Key Laboratory for Resilient Infrastructures of Coastal Cities (Shenzhen University), Ministry of Education, Shenzhen, China, e-mail: biaohu3-c@szu.edu.cn

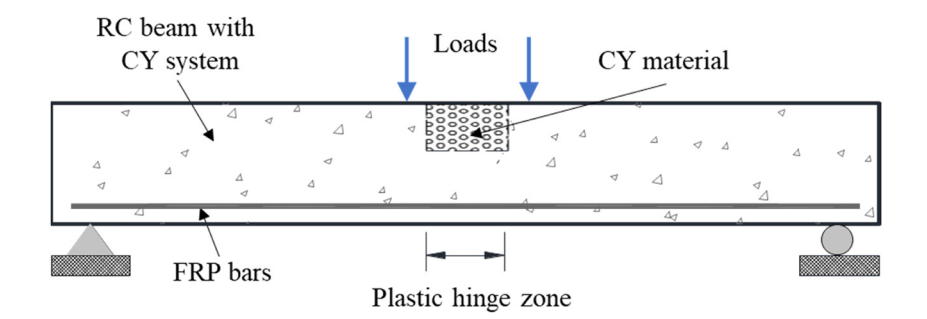


Figure 1: RC beam incorporating CY system [19].

to simultaneously use the full strain capacity of concrete and FRP bars. Although the above-stated approaches are effective at certain levels, they are considered either too complicated or not very effective [9,10]. To facilitate the use of FRP bars (or other material showing linear elastic behavior under tension like high-strength steel) in concrete beams, the ductility demand must be satisfied.

It is well known that for normal steel-concrete structural components, the ductility is contributed by the formation of a plastic hinge due to the tensile elongation of steel bars after yielding [11-13]. Thus, the FRP bar-concrete structures cannot reach satisfactory ductility using the traditional structural concept. However, a new structural system called compression yield (CY) has been proposed by Wu [10,14] to solve the ductility deficiency of flexural members reinforced with non-ductile reinforcing bars. The mechanism behind the CY concept is straightforward: the compression-zone concrete in the plastic hinge is replaced by a kind of material that can reach very large strain but with the strength maintained, which makes it possible that the formation of the plastic hinge is contributed by the compression yielding on the compression side rather than through the yielding of the reinforcement on the tension side. The structural concept and configuration of an RC beam with a CY system are illustrated in Figure 1. More systematic experimental and analytical investigations have been carried out elsewhere [15-17].

The development of a CY material is the most crucial part of implementing the CT structural system. The slurry infiltrated fiber concrete [18] and specially treated metal [19] are two kinds of materials that can reach enhanced ductility and strength. However, both of them are far away from meeting the requirements of a CY material. Motivated by the technology of perforation [15], in this work, a perforated mild steel block is developed to act as the CY material. By optimizing the size and layouts of perforations, the block can deform until it reaches

extraordinarily large strain capacity with the strength maintained. Through experimental, numerical, and analytical investigations, key parameters that influence the stress-strain responses of perforated steel block are identified. Based on the database obtained via finite element (FE) simulations and tests, theoretical formulae for the predictions of modulus of elasticity, ultimate strength and stress-strain curves are developed in the paper.

2 Experimental program

2.1 Test details

All the specimens in this test were made of the same batch of low-carbon steel (Q235A, with a yield strength of 235 MPa), including two solid cuboids and ten perforated cuboid specimens. The physical diagram of the specimens is shown in Figure 2. The main purpose of the two

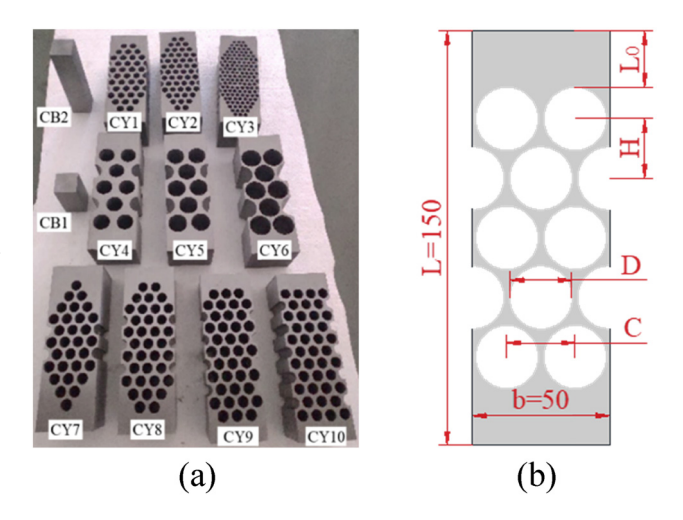


Figure 2: Test specimens (a) CY block (b) dimensions.

solid blocks (with the dimensions [length \times width \times height] of $25 \,\mathrm{mm}^3 \times 25 \,\mathrm{mm}^3 \times 50 \,\mathrm{mm}^3$ and $25 \,\mathrm{mm}^3 \times$ $25 \, \text{mm}^3 \times 100 \, \text{mm}^3$) is to measure the yield strength of the material itself under compression. For the 10 perforated specimens, all with the dimensions (length \times width \times height) of $25 \text{ mm}^3 \times 25 \text{ mm}^3 \times 50 \text{ mm}^3$, the ratio of height-to-width was 3.0. The test variables including the aperture *D*; the distance of two adjacent holes in the horizontal direction (C); the perforation ratio r(r = D/C); the hole pattern coefficient h (h = H/C); and the wedge pattern of the hole arrangement $(\phi = m/n)$ were considered. The parameter m is the number of holes at the first layer and the parameter n is the maximum value of the hole number at one layer around the middle height of a specimen. The two solid specimens were named CB1 and CB2, and the 10 perforated specimens were simply signified as CY1 to CY10 in sequence, as shown in Figure 2. The details of the test specimens are summarized in Table 1.

The load-displacement responses of CB1 and CB2 are shown in Figure 3, indicating that the yielding loads of both specimens were around 173 kN, corresponding to a yielding strength of about 277 MPa. The loading actions for specimens CB1 and CB2 were terminated at loads of 500 and 400 kN, respectively. A universal testing machine with a loading capacity of 3,000 kN was utilized to apply static axial compression load and a displacement control loading manner was adopted with a loading rate of 2 mm/min. For the instrumentations, the strain fields of specimens were monitored and recorded by a digital image correlation (DIC) system (Resolution: 5 mega-pixel; Camera type: Schneider-KREUZNACH 2.0/ 28-0901; Digital correlation software: Vic-3D) which has been demonstrated to be accurate in terms of measuring

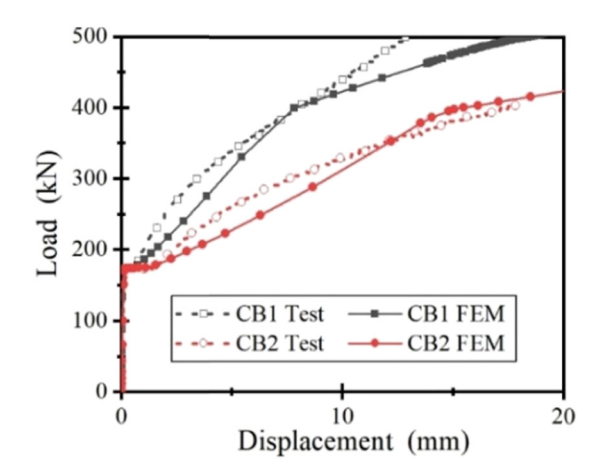


Figure 3: Load-displacement curves of CB1 and CB2.

strain fields of concrete [20–22], engineered cementitious composite (ECC) [10], and FRP laminates [1,8]. The distance between the DIC cameras and the specimen was around 1,000 mm. In addition, two linear variable differential transformers (LVDTs; Type: YWC-50; Precision: 0.01 mm) were adopted to measure the vertical deformation of a specimen. The test setup and instrumentations are illustrated in Figure 4.

2.2 Test results and analyses

The stress-strain responses of all specimens are shown in Figure 5. Some key points on stress-strain curves and other typical indicators for performance evaluations are summarized in Table 1. As expected, all the specimens

Table 1: Specimen details

Spec. ID	D (mm)	<i>C</i> (mm)	<i>H</i> (mm)	r	φ	h	$\sigma_{\rm y}~({ m MPa})$	$\sigma_{\rm p}~({ m MPa})$	ε _y (%)	$\boldsymbol{arepsilon}_{\mathrm{p}}$ (%)	$\boldsymbol{\varepsilon}_{u}$ (%)	λ	μ
CB1	_	_	_	_	_	_	_	_	_	_	_	_	_
CB2	_	_	_	_	_	_	_	_	_	_	_	_	_
CY1	8.75	12.5	10.825	0.7	2/4	0.866	70	130	0.13	8.1	11.5	0.54	62
CY2	8	10	10	0.8	2/5	1.0	70	143	0.09	7.2	15.5	0.49	172
CY3	5	6.25	6.25	0.8	3/8	1.0	62	95	0.1	2.3	4.2	0.65	42
CY4	17.5	25	21.65	0.7	2/2	0.866	70	142	0.12	20	24	0.49	200
CY5	20	25	21.65	0.8	2/2	0.866	40	62	0.14	5.5	19.5	0.65	139
CY6	22.5	25	21.65	0.9	2/2	0.866	12	16	0.13	3	18	0.88	138
CY7	10	12.5	10.825	0.8	1/4	0.866	55	94	0.12	5.3	12	0.59	100
CY8	10	12.5	10.825	0.8	2/4	0.866	46	90	0.12	6	14	0.51	117
CY9	10	12.5	10.825	0.8	3/4	0.866	45	85	0.13	6	12	0.53	92
CY10	10	12.5	10.825	0.8	4/4	0.866	44	85	0.13	7	24	0.52	185

Note: D = aperture; C and H = hole distance in vertical direction and horizontal direction; r = D/C; $\phi = m/n$; m = the hole number at the firstlayer; $n = \text{maximum values of the hole number at one layer; } h = H/C; \sigma_v \text{ and } \varepsilon_v = \text{yield strength and strain; } \sigma_v \text{ and } \varepsilon_v = \text{peak strength and } s$ corresponding strain; ε_u = ultimate strain; yield-to-peak stress ratio $\lambda = \sigma_v/\sigma_p$; ductility ratio $\mu = \varepsilon_u/\varepsilon_v$.

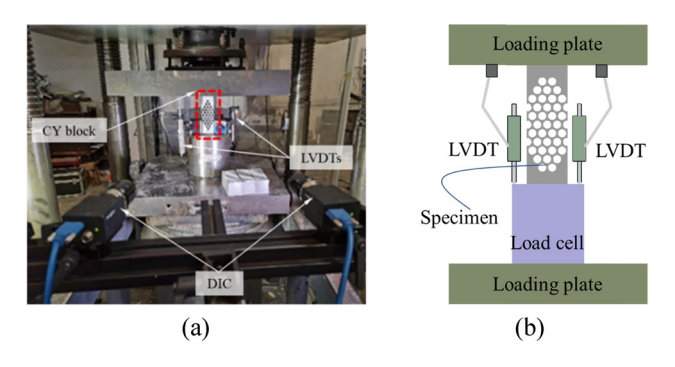


Figure 4: Test setup (a) loading protocol and DIC system (b) schematic.

showed a large post-yield strain (deformation) capacity, indicating the effectiveness of perforation in terms of increasing member ductility. Besides, compared with the solid steel block, some perforated specimens (e.g.,

CY3, CY5, and CY6) are also characterized by relatively large yield-to-peak stress ratio (λ), indicating that the stress experienced a small increase at very large member inelastic strain (deformation). For almost all the perforated specimens, after the first peak stress, the stress experienced a certain degree of fluctuation under increasing strain. The decreased stress is due to the gradual compression of the void as well as the buckling of the thin-walled steel skeleton after perforation and the squashed perforations enable the stress to start to increase again, as clearly depicted in Figure 6.

The ductility ratio μ , defined by $\varepsilon_u/\varepsilon_y$, of each specimen is summarized in Table 1. The yield strain and ultimate strain are represented by ε_y and ε_u , respectively. Two situations were used for the determination of the ultimate point. First, the point where the stress reached the first peak stress σ_p for the second time can be viewed

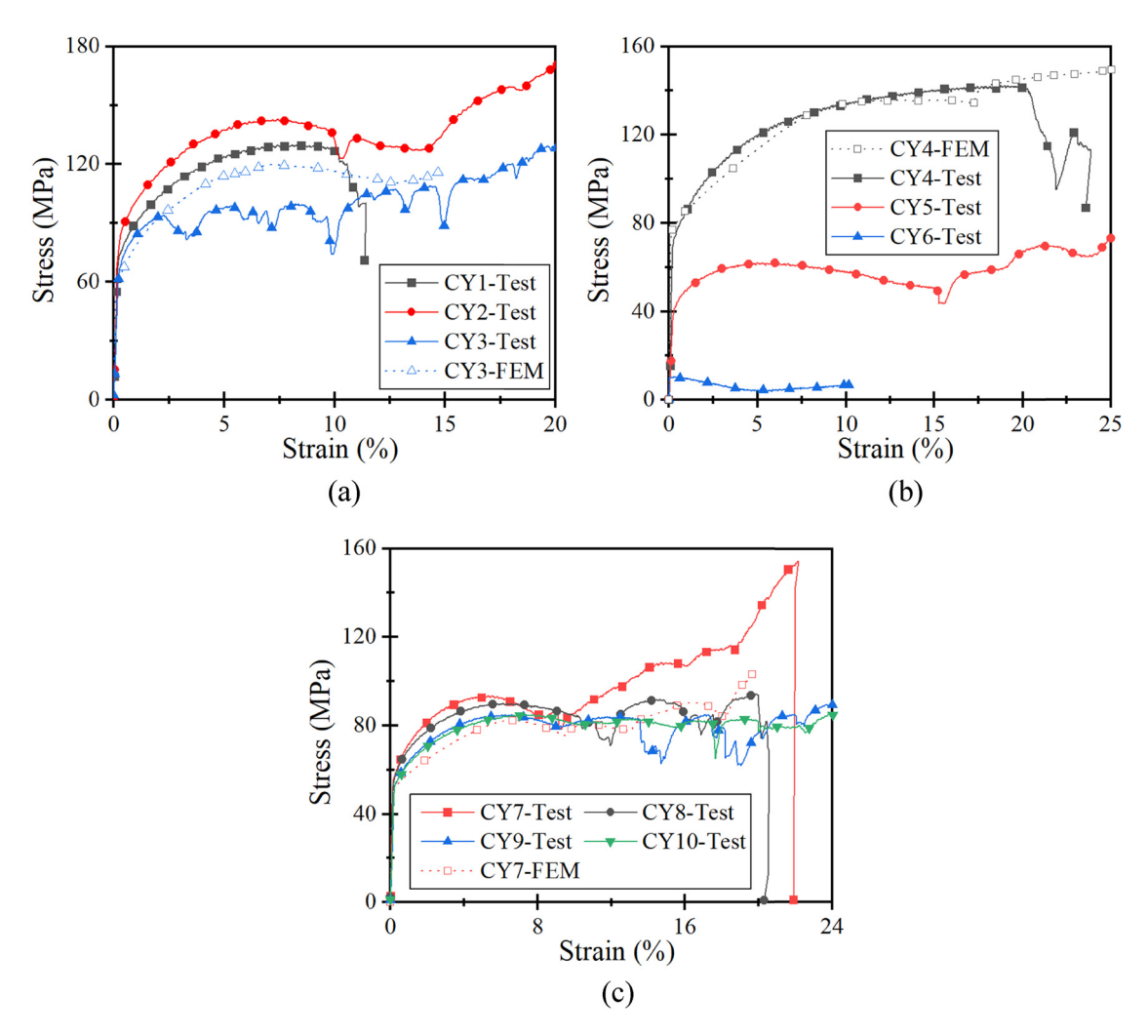


Figure 5: Stress-strain responses: (a) specimens CY1, CY2, and CY3; (b) specimens CY4, CY5, and CY6; (c) specimens CY7, CY8, CY9, and CY10.

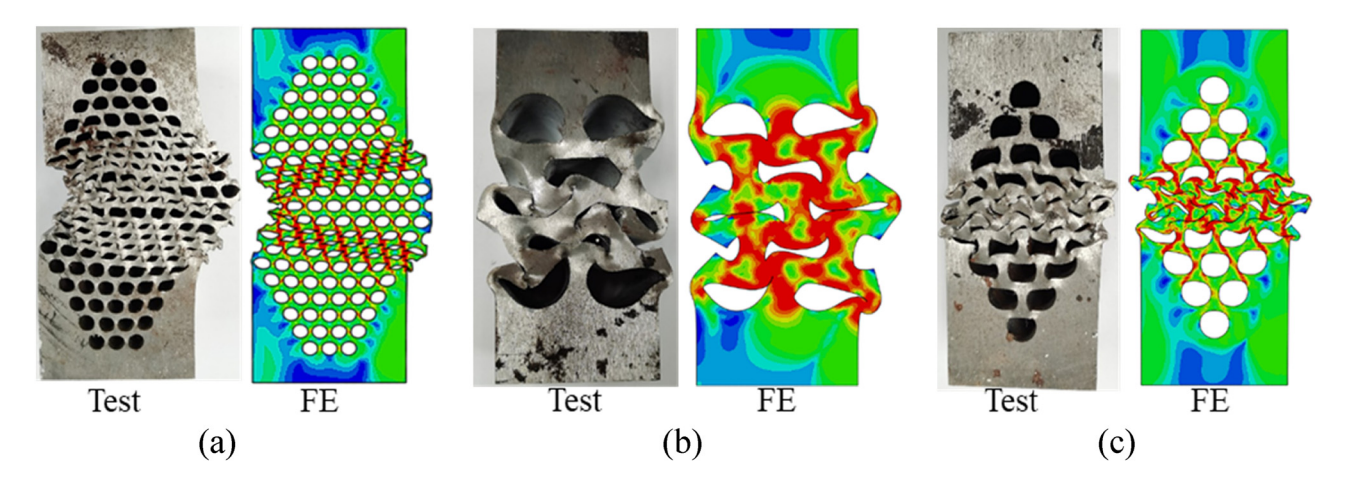


Figure 6: Typical failure modes: (a) specimens CY3; (b) specimens CY4; and (c) specimens CY7.

as the ultimate point. Second, the stress continuously decreases after the first peak σ_p and the point where the stress dropped sharply is taken as the ultimate point. The ductility ratios of most specimens were close to or larger than 100, which can be viewed as extraordinary because a ductility demand of more than ten times the ductility demand of a beam was required for the CY material [14]. Typical failure modes include outward buckling, global squash, and local squash, as illustrated in Figure 6(a)–(c), respectively. Outward buckling (specimen CY3) and global squash (specimen CY4) will result in a relatively flat stress-strain curve after the first peak stress whereas local squash (specimen CY7) can enable the specimen to carry increased stress due to the direct support of the wedge-shape solid steel at specimen ends. Besides, the key variables including hole arrangement (h), void ratio (r), hole diameter (D), and hole arrangement shape at specimen ends (ϕ) exert influence on the stress-strain responses and failure modes of perforated steel blocks, which will be systematically investigated using FE simulations subsequently.

3 FE simulation and model calibration

The general FE software ABAQUS [23] is used in the current work to conduct parametric studies and to form a database of material responses. The two-dimensional FE model, with the boundary conditions the same as that occurring in tests, was adopted to simulate the behavior of perforated steel blocks to enhance the understanding of mechanical responses of perforated steel blocks under a large range of parameters. The CPS4R solid elements

were used in the FE model. Surface contacting actions in the normal and tangential directions were considered to simulate the actual behaviors of squashed voids. Hard contact was utilized to consider the normal action, which transfers the compression force only with the tensile force neglected. In tangential direction, interfacial friction force triggered between the squashed steel walls once later uneven deformation occurs, the effects of which are approximated as per the penalty function of the Coulomb friction model in ABAQUS as the friction law. The frictional coefficient is set as 0.1 in the FE simulation, as suggested by Xiao and Ma [24]. The constitutive law proposed by Han [25] was used to represent the stress-strain relationship of steel, as shown in Figure 7. The yield strength (σ_{v}) , the initial modulus of elasticity $(E_{\rm s})$, and the Poisson's ratio (ν) are 277 MPa, 210 GPa, and 0.27, respectively. The ultimate stress $\sigma_{\rm u}$ equals $2\sigma_{\rm v}$, and the fracture strain of steel is set as 0.5. After a comparison of simulations adopting various mesh sizes, a mesh size of around 2 mm was eventually adopted in the FE models.

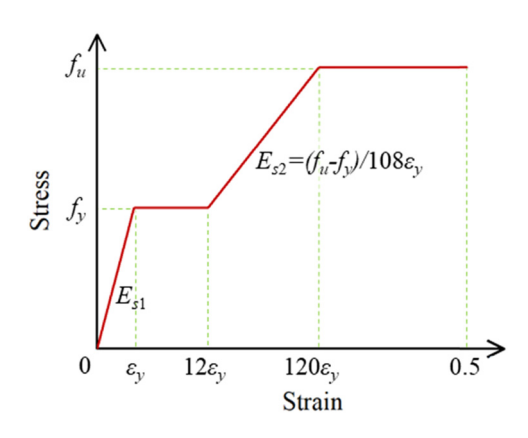


Figure 7: Constitutive law of steel proposed by Han [31].

The FE models are calibrated from three aspects, i.e., the material behavior (Figure 3), the stress–strain responses of perforated steel blocks (Figure 5), and failure mode of a steel block with perforations (Figure 6). Generally, the load-displacement curves obtained in tests and FE simulations agree well with each other, as shown in Figure 3. As depicted in Figure 5, variation trends of stress-strain responses obtained from simulations and tests are similar and the errors of yield and ultimate strength are smaller than 10%. With regard to the failure modes, outward buckling, global squash, and local squash that are observed in tests are well captured by the FE simulations, as illustrated in Figure 6. Therefore, the FE models are reasonably accurate in terms of predicting the mechanical performance of perforated steel blocks and subsequently, these models will be used to conduct parametric studies.

4 Parametric study

4.1 Effect of hole number per layer n

Under the same void ratio r, a larger n value results in a smaller hole diameter (or more distributed holes) and *vice versa*. In this section, five n values are selected, namely 2, 3, 4, 5, and 6, and the other parameters r, h, L_0/L , and ϕ are set as 0.8, 0.866, 0.14–0.18, and 1.0, respectively. The arrangement of holes under the above-stated parameters is shown in Figure 8. It can be seen from Figure 9 that the number of holes per layer exerts a certain influence on the elastic stiffness E_1 and the peak strength $\sigma_{\rm u}$. The E_1 and $\sigma_{\rm u}$ values increase with increasing n values until the n value reaches around 4. Further increase of

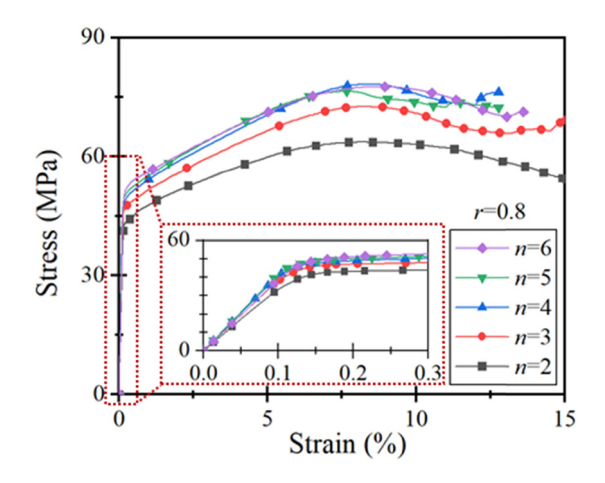


Figure 9: Effect of hole number per layer n.

n exerts negligible influence on the stress–strain curve of members. Therefore, in the subsequent parameterized model of perforated steel block, the case with an n value of 4 is taken as the benchmark. For a member with an n value of 2, a coefficient of 0.85 is considered for both E_1 and σ_u with respect to that of a member with an n value of 4, and this coefficient changes to 0.95 for the member with an n value of 3. For members with n values greater than 4, no reduction factors are considered.

4.2 Effect of wedge-shape coefficient ϕ at member end

For anchor purposes in a perforated steel block in a CY structural system, a certain length of anchoring solid area is needed to be preserved, which will inevitably sacrifice

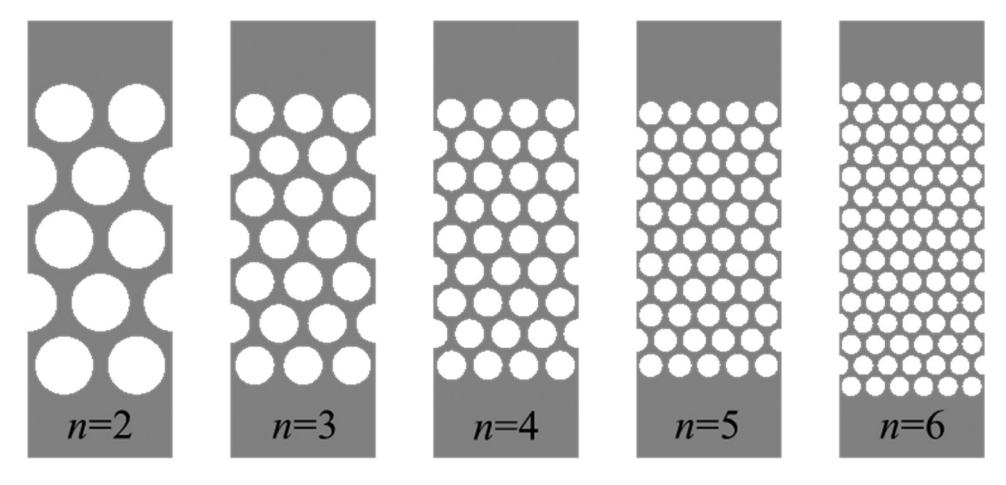


Figure 8: Specimens under different *n* values.

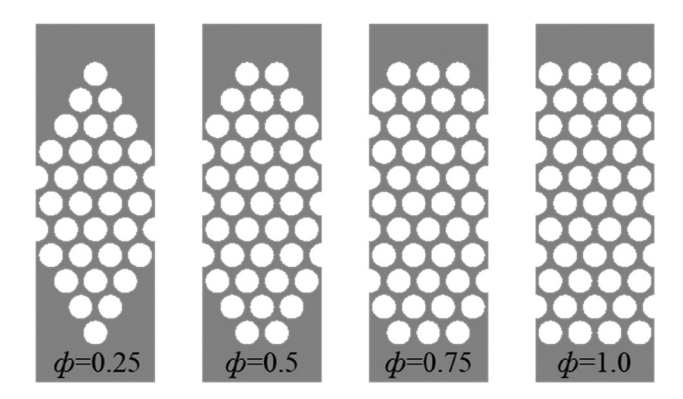


Figure 10: Specimens under different ϕ values.

a certain deformation. In this case, the wedge-shaped hole arrangement at the ends can provide a certain solid area for allocating anchors and simultaneously compensate for the deformation loss due to the partial perforations, as shown in Figure 10. Besides, the wedge-shaped solid part is able to provide side support, which in turn postpones or even prevents the outward deformation to enhance member stability. Four wedge-shaped coefficient ϕ values are selected in this section, i.e., 0.25, 0.5, 0.75, and 1.0, and the other parameters n, r, h, and L_0/L are set as 4, 0.866, 0.8, and 0.106–0.219, respectively.

As depicted in Figure 11, for the member with a ϕ value of 0.25, the stress increased greatly when it is loaded to a strain level of about 10%. This increment in stress is because of the wedge-shaped solid region contacted at this strain level, which enables the member to carry further increased applied load. However, this phenomenon is not observed for the other three members and the $\sigma_{\rm u}$ values of these three members (with ϕ values of 0.5, 0.75, and 1.0) are close to each other. Thus, it can be inferred that the effect of the wedge-shaped hole

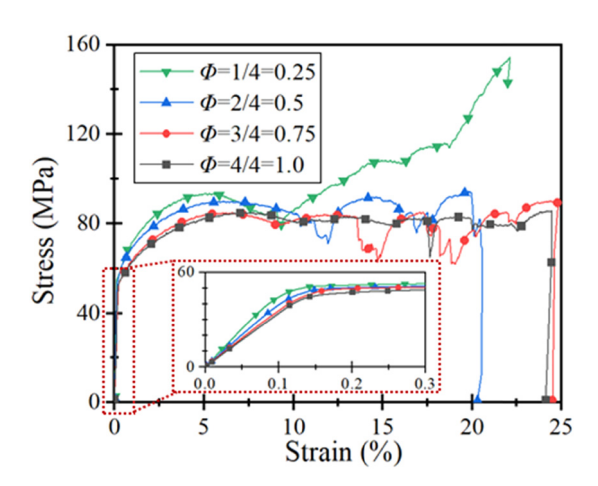


Figure 11: Effect of wedge-shape coefficient ϕ .

arrangement on $\sigma_{\rm u}$ can be ignored if ϕ value is larger than 0.25. On the other hand, it can be seen from Figure 11 that the wedge-shaped hole arrangement at the member ends imposes a certain effect on E_1 . This effect can be equivalently regarded as the change of the perforated length. Thus, the wedge-shaped area at the end can be converted into a solid area according to the area equivalent and the length of the equivalent solid segment L_0 can therefore be obtained, as shown in Figure 12. Thus, different ϕ values correspond to different L_0 and the effect of the equivalent solid segment length L_0 on E_1 will be discussed in detail subsequently.

4.3 Effect of void ratio r

In this section, seven selected r values (i.e., 0.2, 0.4, 0.5, 0.6, 0.7, 0.8, and 0.9) are investigated, and the other parameters (i.e., h = 0.866, $\phi = 1$ and $L_0 \approx 0.04$) are almost the same under varying r, as shown in Figure 13. It can be seen from Figure 14 that void ratio r significantly affects the elastic stiffness and strength. According to best fitting results, the relationship between E_0 and r can be obtained:

$$\frac{E_0}{E_S} = 1.858r^3 - 2.998r^2 + 0.128r + 1,\tag{1}$$

where E_s = elastic stiffness of solid steel block; E_0 = elastic stiffness of perforated steel block without wedge-shaped solid ends. Theoretically speaking, when r equals zero, the specimen is a solid steel block, and E_0 equals E_s . The performance of equation (1) is illustrated in Figure 15(a).

As shown in Figure 13, with other parameters remaining the same, the smaller the r is, the closer the specimen is to the solid block. Thus, the yield strength-to-peak strength ratio decreases sharply with increasing r values (Figure 14), which in turn will significantly deteriorate the ductility

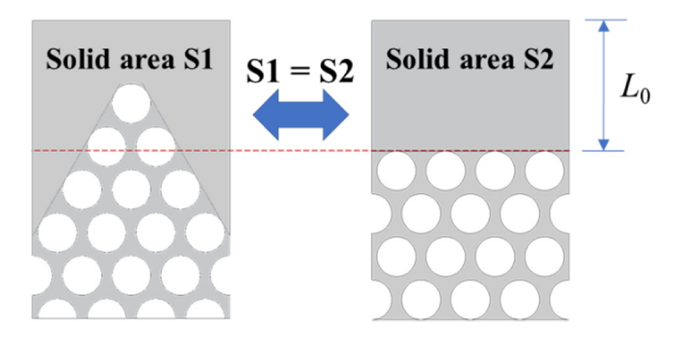


Figure 12: Equivalent conversion of end solid area.

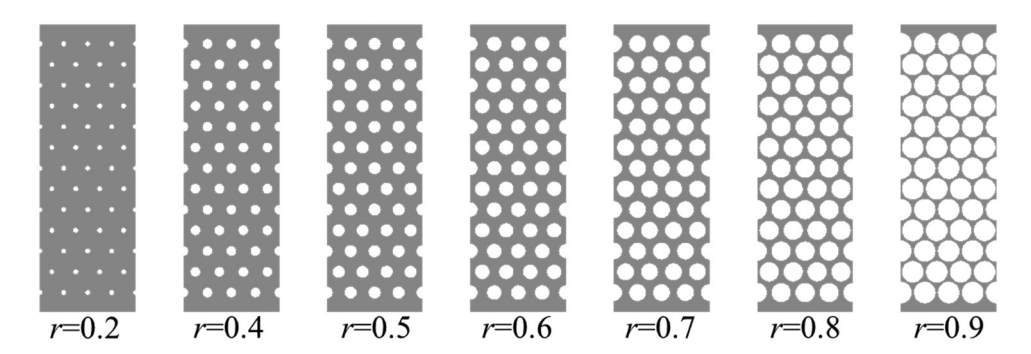


Figure 13: Specimens under different void ratios.

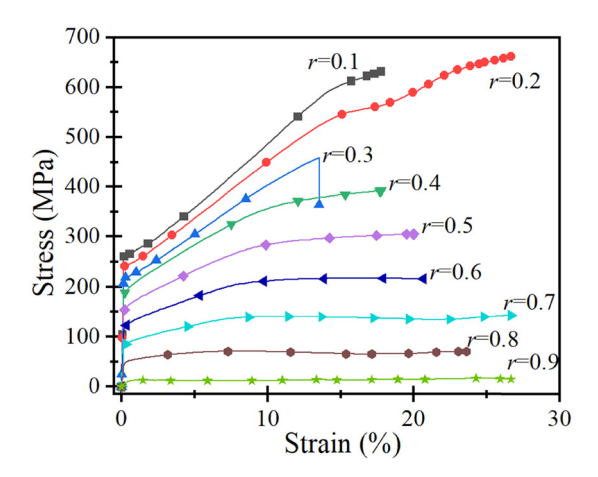


Figure 14: Effect of void ratio *r*.

performance of the CY block and a beam (or column) incorporating the CY structural system [14]. Due to this concern, the void ratio ranging from 0.6 to 0.9 was recommended in the current work. The relationship between the peak stress σ_0

and void ratio *r* can be reached by using fitting the simulation results (Figure 15(b)), which gives

$$\sigma_{\rm u}/f_{\rm y} = 3.2(0.55r^2 - 1.59r + 1).$$
 (2)

Normally, the strength of a perforated block is related to both the material property of steel itself and the geometrical dimensions. Thus, introducing the yield strength of steel f_y (277 MPa) in equation (2) gives the following formula:

$$\sigma_{\rm u} = 3.2 f_{\rm v} (0.55 r^2 - 1.59 r + 1).$$
 (3)

4.4 The effect of solid segment length L_0

The (equivalent) length of the solid segment at the member end (L_0) affects the overall stiffness of perforated steel blocks. The larger the L_0 , the shorter the perforated part, which results in reduced deformation capacity of perforated steel block, as depicted in Figure 16(a). This

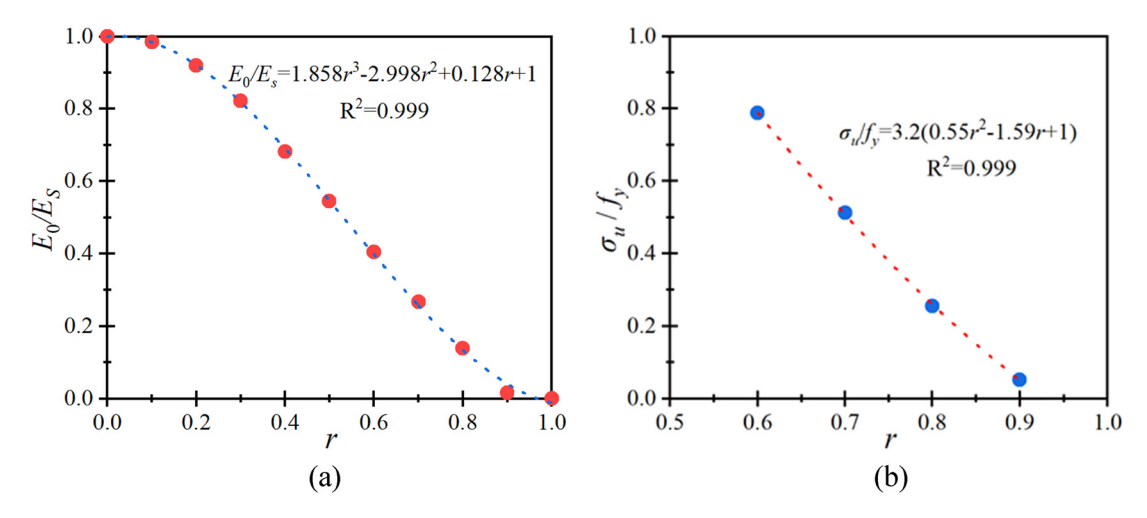


Figure 15: The polynomial fitting results of r on the stiffness and strength (a) effect of r on E_0 (b) effect of r on σ_u .

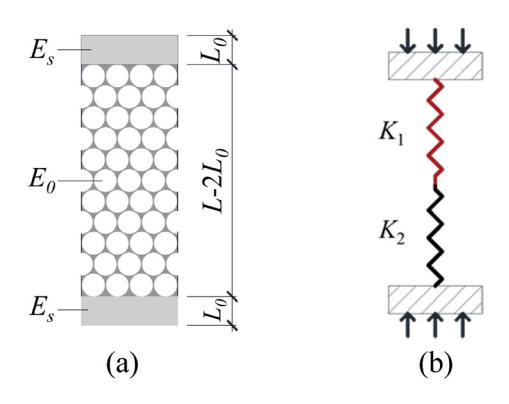


Figure 16: Conceptual model of member stiffness: (a) parameter diagram and (b) conceptual model based on springs.

parameter has a negligible influence on the peak strength due to the localized failure around member middle height but shows a certain impact on the elastic stiffness. As shown in Figure 16(b), the response of a perforated steel block under compression can be regarded as a "spring" series. For a spring, the stiffness can be calculated as K = AE/L, where A, E and L are cross-section area, modulus of elasticity, and member length, respectively. For two springs located in series, the following well-known expression can be used to calculate the total stiffness K:

$$\frac{1}{K} = \frac{1}{K_1} + \frac{1}{K_2},\tag{4}$$

where K_1 and K_2 are the stiffness of two springs in series. As shown in Figure 16(a), $E_{\rm s}$ and E_0 are modulus of elasticity of the pure solid segment and the pure perforated segment, respectively. Thus, in a perforated block with a total length of L, two solid parts with a length of L_0 for each and a perforated part with a length of $L - 2L_0$ exist. Let K_1 and K_2 be the stiffness of the pure solid segment and the pure perforated segment, which yields $K_1 = AE_{\rm S}/2L_0$ and $K_2 = AE_0/(L - 2L_0)$. Let E_1 be the equivalent modulus of elasticity of the whole perforated block as shown in Figure 16(a). Introducing a factor α ($\alpha = E_1/E_{\rm s}$), the following relationship can be obtained:

$$E_{s}A\alpha = E_{1}A = LK = L\frac{K_{1}K_{2}}{K_{1} + K_{2}} = \frac{L\frac{E_{s}A}{2L_{0}} \frac{E_{0}A}{L - 2L_{0}}}{\frac{E_{s}A}{2L_{0}} + \frac{E_{0}A}{L - 2L_{0}}}$$

$$= \frac{LE_{s}E_{0}A}{E_{s}(L - 2L_{0}) + 2E_{0}L_{0}},$$

$$\alpha = \frac{LE_{0}}{E_{s}(L - 2L_{0}) + 2E_{0}L_{0}},$$
(6)

$$\frac{E_0}{E_s} = \frac{\alpha (L - 2L_0)}{L - 2\alpha L_0}.$$
 (7)

Substituting $l_0 = L_0/L$ into equation (7) yields:

$$\frac{E_0}{E_s} = \frac{\alpha (1 - 2l_0)}{1 - 2\alpha l_0}.$$
 (8)

The combination of equations (1) and (8) gives:

$$\alpha = \frac{(1.858r^3 - 2.998r^2 + 0.128r + 1)}{1 + 2l_0(1.858r^3 - 2.998r^2 + 0.128r)}.$$
 (9)

When l_0 equals 0.5, the value of equation (9) is 1.0, indicating that E_1 equals E_s . On the other hand, $l_0 = 0.5$ means that the length of the perforated segment is zero and the specimen is a solid steel block (Figure 16(a)), which naturally results in the case of $E_1 = E_s$.

For two groups of specimens with different L_0 and r values with other parameters being the same, the calculated α values as per equation (9) are compared with that of the FE simulations (Figure 17). It is found that equation (9) predicted values agree well with the FE simulated ones.

4.5 Effect of hole arrangement coefficient h

In this section, the influence of five hole arrangement coefficient h values (1, 0.886, 0.8, 0.75, and 0.7) are investigated under different r values (0.6, 0.7 and 0.8), and Figure 18 shows the specimen details. It can be seen from Figure 19 that under the same r, a CY block with a larger h value can reach a much higher ultimate bearing capacity compared with that of a CY block with a smaller h, but the elastic limit of the two cases is close. For example, it can be found that the CY block with h = 0.8 can obtain a larger yield strength-to-peak strength ratio than the CY block with h = 1.0, which is more in line with the ideal requirement of CY block used as the structural fuse [26]. Thus, it can be inferred that a smaller h will

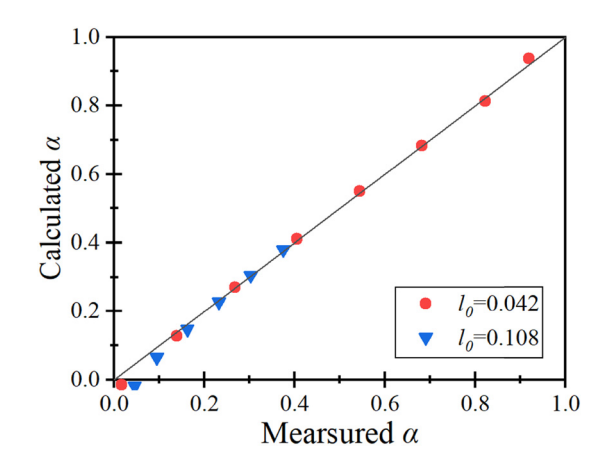


Figure 17: Comparison between equation (9) prediction and FE simulation.

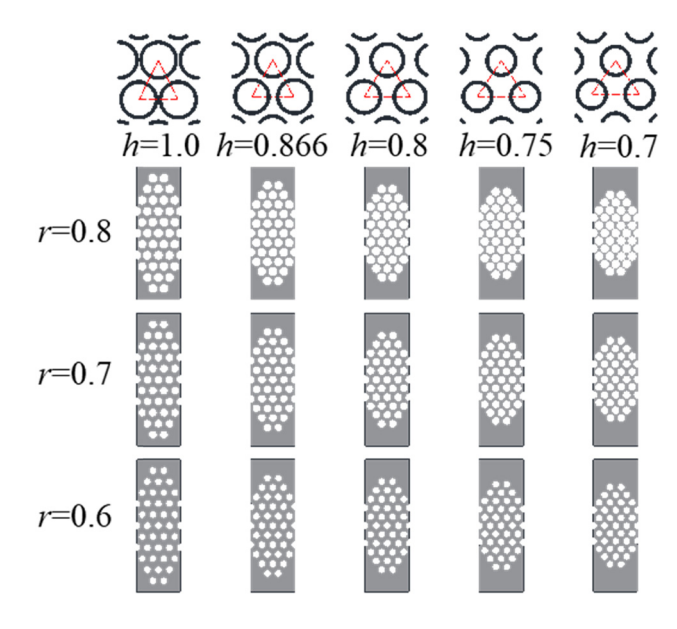


Figure 18: Specimens under different h.

further reduce the yield strength-to-peak strength ratio. Besides, a relatively larger yield strength-to-peak strength ratio needs a much smaller h value (Figure 19(c)) if the r value is too small (e.g., lesser than 0.6).

Under the same r value, the peak stress σ_u is almost linearly proportional to the value of h, as depicted in Figure 20(a). To quantify the influence of the h value on σ_u , the σ_u of all CY blocks is divided by the σ_u of the CY block with the same r and an h value of 0.866, as shown in Figure 20(b). Illustrated in Figure 20(c) is the slope k of each curve shown in Figure 20(b). If the void ratio r equals 0 and the h value exerts no influence on σ_u , it means that the slope is zero. Thus, as shown in Figure 20(c), the fitting of four points gives the expression of k against r. Herein, assuming h_σ to be the strength adjustment coefficient of σ_u with respect to the member with h value of 0.886, that is:

$$\sigma_{\rm u} = h_{\sigma} \sigma_{\rm u(h=0.866)}, \tag{10}$$

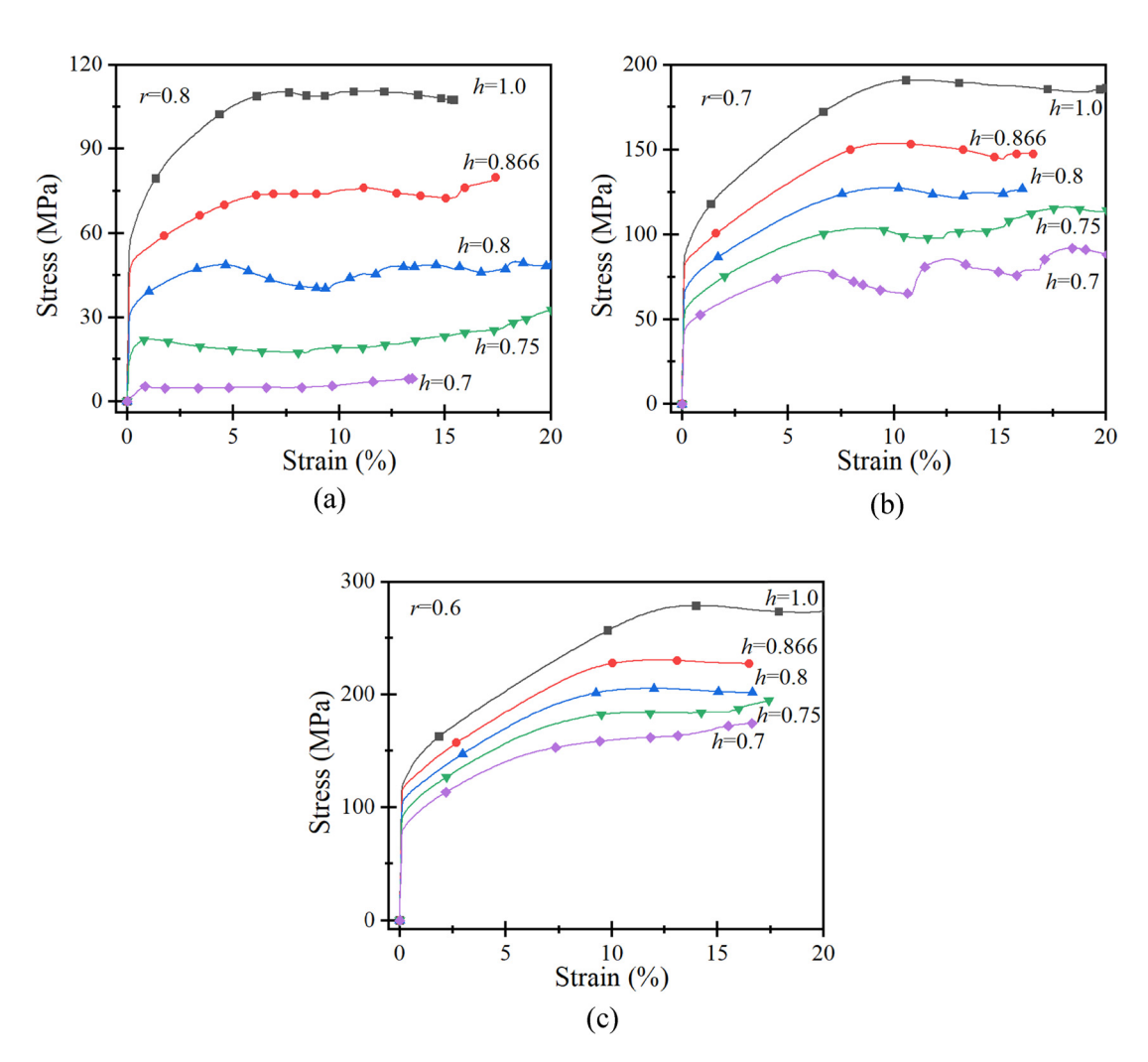


Figure 19: Effect of h: (a) effect of h under an r value of 0.8; (b) effect of h under an r value of 0.7; and (c) effect of h under an r value of 0.6.

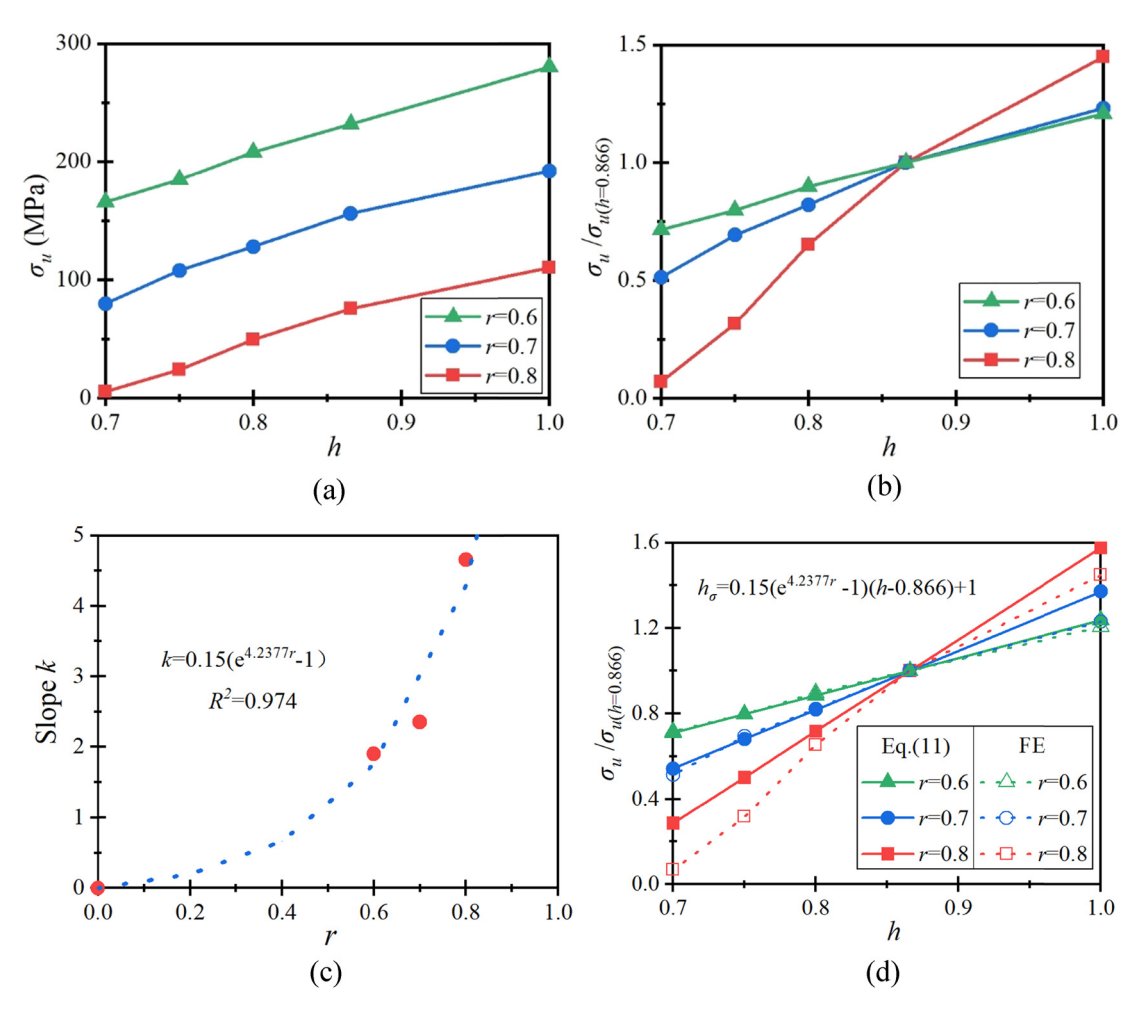


Figure 20: The strength adjustment coefficient h_e (a) effect of h on σ_u (b) effect of h on $\sigma_u/\sigma_{u(h=0.886)}$ (c) effect of r on k (d) performance of fitted results.

where the expression of h_e can be obtained by fitting results:

$$h_{\sigma} = 0.15(e^{4.2377r} - 1)(h - 0.866) + 1.$$
 (11)

The performance of equation (11) is shown in Figure 20(d), and accurate predictions can be found.

As shown in Figure 21(a), under the same r value, the E_1/E_s increases almost linearly with increasing h. To model the influence of the h value on E_1 , under the same r values, E_1 of each CY block is divided by E_s of the CY block with an h value of 0.866 ($E_1/E_{s(h=0.886)}$), as shown in Figure 21(b). The slope (k) values of the three curves shown in Figure 21(b) can be calculated. Under the case of r=0, the specimen is a solid block and the E_1 is a constant ($E_1=E_s$), which results in k=0. Fitting these four points yields the expression of k, as shown in Figure 21(c). Similar to σ_u , a modulus of elasticity adjustment coefficient of h_e is introduced with respect to the member with h value of 0.886, which gives:

$$E_1 = h_e E_{1(h=0.866)}. (12)$$

Similarly, the equation of $h_{\rm e}$ can be obtained by data fitting, that is,

$$h_{\rm e} = 0.05({\rm e}^{5.4037r} - 1)(h - 0.866) + 1.$$
 (13)

The performance of equation (13) is shown in Figure 21(d), wherein good agreement can be found between the simulations and analytical equations. However, certain differences can be found for the cases where r value equals 0.8 and h values are smaller than 0.8, in which case, the strength and stiffness (e.g., E_1/E_s smaller than 0.3) are too small.

4.6 Yield strength-to-peak strength ratio λ

The yield strength-to-peak strength ratio is expressed as $\lambda = \sigma_y/\sigma_u$. For an ideal CY block, it is hoped that the value

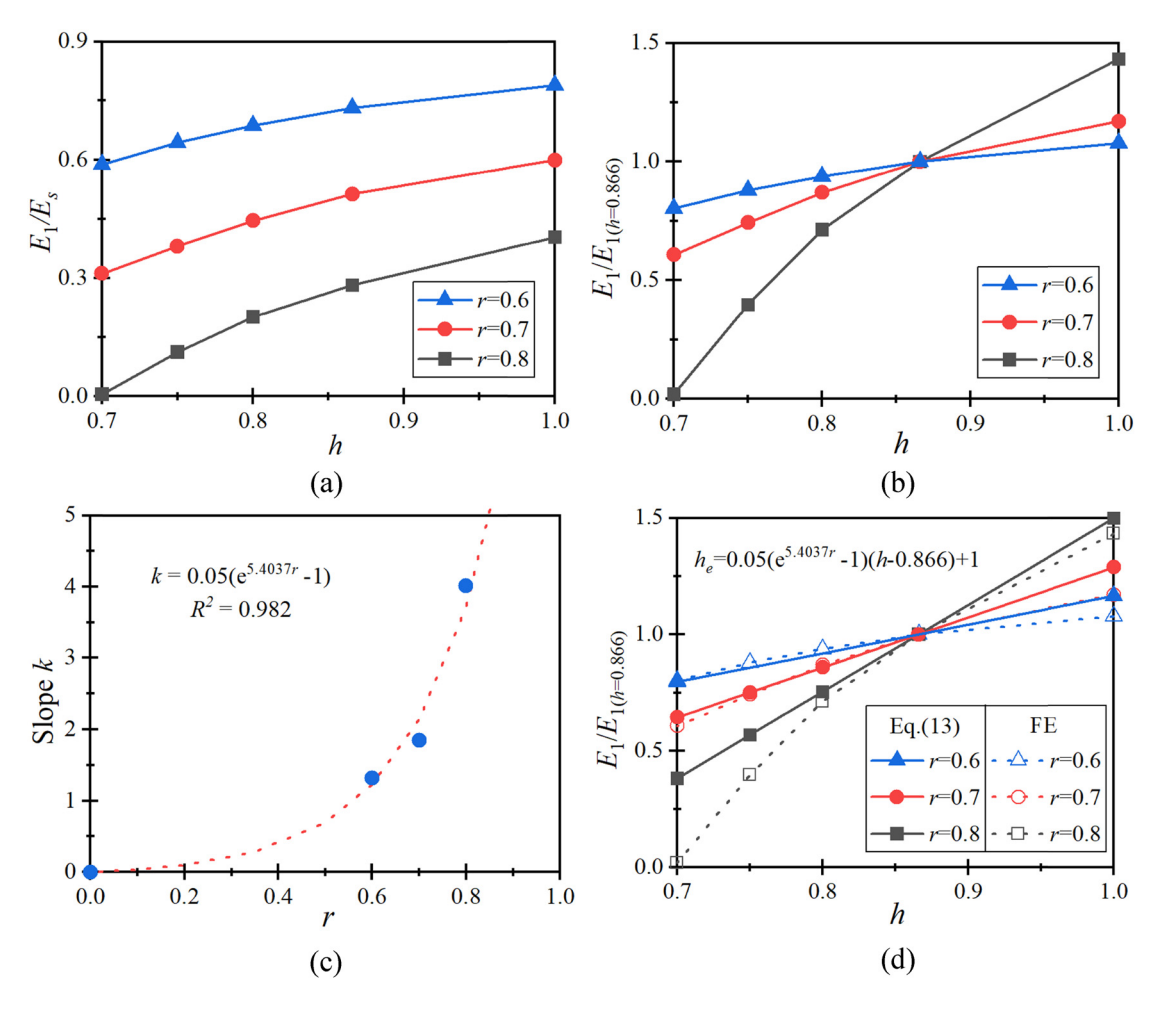


Figure 21: The strength adjustment coefficient h_e : (a) effect of h on E_1/E_s ; (b) effect of h on $E_1/E_{1(h=0.886)}$; (c) effect of r on k; and (d) performance of fitted results.

of δ will be as close as possible to 1.0 [15]. It can be seen from the stress-strain responses of CY blocks that the λ are closely related to void ratio r and hole arrangement coefficient h. With the increase of h, the stiffness and strength increase but the λ decrease. With the increase of r, the yield strength increases, while the strength decreases, which results in the increase of λ . An inappropriate r value contributes to negative effects on the yield strength-to-peak

Table 2: Values of λ

	,	r							
	λ	0.6	0.7	0.8	0.9				
	1	0.43	0.47	0.5	0.7				
	0.866	0.48	0.52	0.63	0.75				
Н	0.8	0.49	0.53	0.67	0.8				
	0.75	0.5	0.54	0.76	0.85				
	0.7	0.51	0.58	0.9	0.95				

strength ratio of a CY block. According to the statistics of test data, it is suggested that the values of yield strength-to-peak strength ratio λ can be determined according to Table 2. The linear interpolation can be used for some cases where the h and r values cannot be found in Table 2.

5 Stress-strain model of perforated blocks

5.1 Model features

As shown in Figure 22, the most prominent feature of the stress-strain curve of a typical CY block is that the curve consists of a straight line segment with complete elasticity at the beginning and a curve segment with a large plastic strain. The two most important mechanical

parameters of the curve are the stiffness at the elastic stage and the peak strength at the plastic stage. Therefore, in this section, the expressions of these two parameters (E_1 and $\sigma_{\rm u}$) will be obtained by combining data statistics with theoretical derivations. Finally, based on the developed equations for E_1 and $\sigma_{\rm u}$, a suitable mathematical model is selected to establish the complete stress—strain model of the CY block under compression.

5.2 The expression of E_1

Combining equations (9) and (13) gives the expression of E_1 , which is

$$E_{1} = E_{s} \alpha_{(h=0.866)} h_{e}$$

$$= E_{s} \left[\frac{(1.858r^{3} - 2.998r^{2} + 0.128r + 1)}{1 + 2l_{0}(1.858r^{3} - 2.998r^{2} + 0.128r)} \right]$$

$$\times \left[0.05(e^{5.4037r} - 1)(h - 0.866) + 1 \right].$$
(14)

Notably, in equation (14), only r and h are included in the parametric formula, and the effect of hole number per layer n on the E_1 has been stated in Section 4.1. As observed previously in both tests and simulations, at the end of the elastic stage, there is a gently hardening portion represented by a segment of a curve. The initial slope of this hardening stage is denoted by E_2 (Figure 22). The relationship between E_1 and E_2 can be statistically and empirically obtained according to the simulation data and test results, and finally, a simple expression is found to describe their relationship, which is

$$E_2 = 0.015E_1. (15)$$

5.3 Expression of $\sigma_{\rm u}$

As stated in Section 4.3, it is reasonably deduced that the peak stress $\sigma_{\rm u}$ is related to both material properties and geometrical dimensions. Herein, using a non-dimensional factor β (related to member geometrical properties) and material property $f_{\rm y}$ to represent $\sigma_{\rm u}$:

$$\sigma_{\rm u} = f_{\rm v}\beta = f_{\rm v}\beta_{(h=0.866)}h_{\sigma}.$$
 (16)

A combination of equations (3) and (11) results in the following expression:

$$\sigma_{\rm u} = f_{\rm y}\beta = 3.2f_{\rm y}(0.55r^2 - 1.59r + 1) \times [0.15(e^{4.2377r} - 1)(h - 0.866) + 1].$$
 (17)

Notably, only r and h are included in the parametric equation (17) and the effect of hole number per layer n on $\sigma_{\rm u}$ is discussed and presented in Section 4.1.

5.4 Parametric models

To facilitate the process of development of the stress–strain equations, three slopes are introduced, namely k_1 , describing the slope of the elastic stage; k_2 , denoting the initial slope of strain hardening part; and k_3 , representing the slope of the curve at large (infinite) strain, as shown in Figure 23. The first section is the straight-line part of the elastic stage, the second section is the secondary hardening, and thereafter yield platform stage.

For the elastic phase ($\varepsilon \le \varepsilon_0$), the following simple equation can be obtained:

$$\sigma(\varepsilon) = k_1 \varepsilon. \tag{18}$$

For the inelastic stage ($\varepsilon > \varepsilon_0$), a four-parameter model [27] is adopted to describe the curve, which is

$$\sigma(\varepsilon) = A\left(e^{-\frac{\varepsilon}{B}} + C + D\varepsilon\right)\left(1 - e^{-\frac{\varepsilon}{B}}\right),\tag{19}$$

where A, B, C, and D will be determined subsequently. In the following derivation, according to Figure 23, the point $(\varepsilon_0, \sigma_y)$ is viewed as the original point of the local coordinate system.

When ε approaches a large enough value, equation (19) becomes

$$\sigma(\varepsilon) = AD\varepsilon + AC = \sigma_u - \sigma_y. \tag{20}$$

According to Figure 23, at large enough strain value, the following equations can be reached:

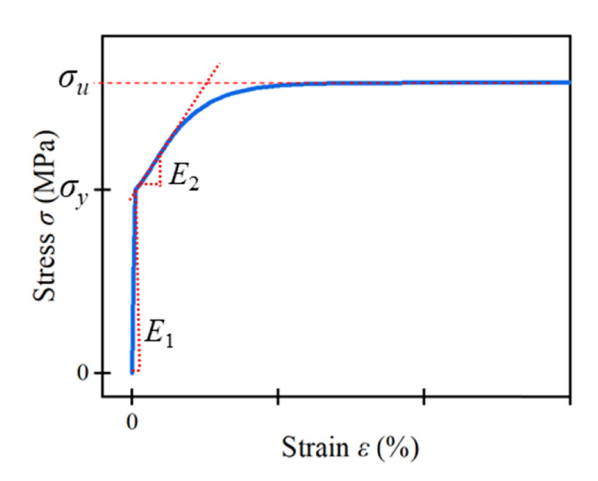


Figure 22: Typical stress-strain response.

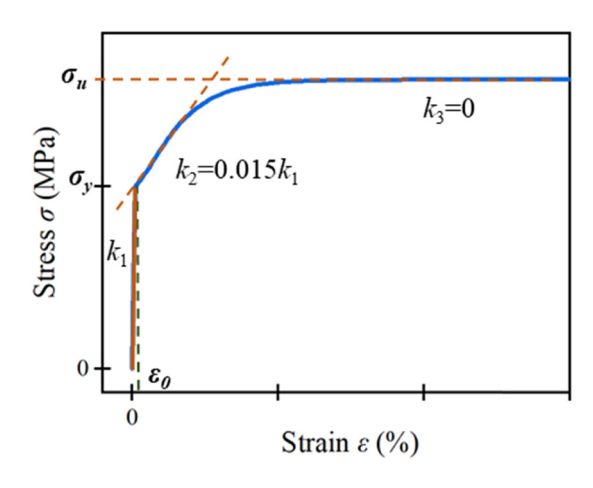


Figure 23: Schematic of the stress-strain model.

$$AD = k_3 = 0,$$
 (21)

$$AC = \sigma_u - \sigma_v. \tag{22}$$

Differentiating equation (19) with respect to ε and letting $\varepsilon=0$ yields:

$$\sigma'(\varepsilon)|_{\varepsilon=0} = k_2 = \frac{A}{B}(C+1). \tag{23}$$

The combination of equations (22) and (23) gives the expressions of A and C:

$$A = k_2 B + \sigma_{\rm v} - \sigma_{\rm u}, \tag{24}$$

$$C = \frac{\sigma_{\rm u} - \sigma_{\rm y}}{k_2 B + \sigma_{\rm y} - \sigma_{\rm u}}.$$
 (25)

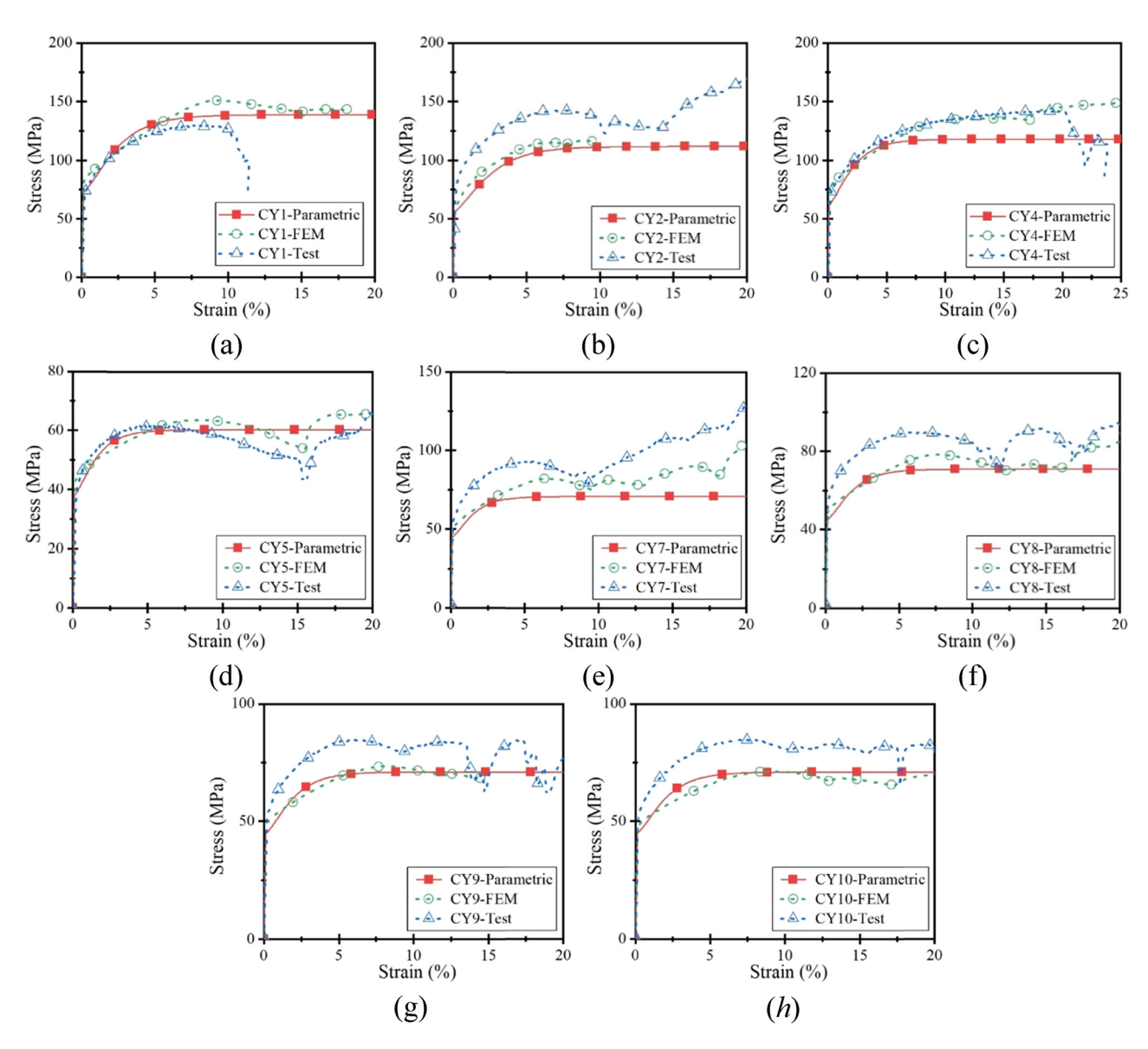


Figure 24: Calibration of the parametric model using test results and FE predictions: (a) CY1, (b) CY2, (c) CY4, (d) CY5, (e) CY7, (f) CY8, (g) CY9, and (h) CY10.

According to Zhou and Wu [27], the assumed shape of the stress–strain curve necessitates $C \ge 1$. Substituting $C \ge 1$ into equation (25) yields:

$$B \le \frac{2(\sigma_{\mathbf{u}} - \sigma_{\mathbf{y}})}{k_2}.\tag{26}$$

Let $B = \varepsilon_n = f\varepsilon_1$ and $\varepsilon_1 = 2(\sigma_{\rm u} - \sigma_{\rm v})/k_2$, equation (26) is equivalent to $f \le 2$. Substituting $B = \varepsilon_n$ and equations (21), (22), and (24) into equation (19) gives:

$$\sigma(\varepsilon) = \left[(k_2 B + \sigma_y - \sigma_u) e^{-\frac{\varepsilon}{\varepsilon_n}} + \sigma_u - \sigma_y \right] \left(1 - e^{-\frac{\varepsilon}{\varepsilon_n}} \right). (27)$$

Substituting $B = \varepsilon_n = f\varepsilon_1$ and $\varepsilon_1 = 2(\sigma_u - \sigma_v)/k_2$ into equation (27) and offsetting the original point of the local coordinate system to point $(\varepsilon_0, \sigma_v)$ in the global coordinate system yields:

$$\sigma(\varepsilon) = (\sigma_{u} - \sigma_{y}) \left[(f - 1)e^{\frac{-\left(\varepsilon - \frac{\sigma_{y}}{k_{1}}\right)k_{2}}{f(\sigma_{u} - \sigma_{y})}} + 1 \right]$$

$$\times \left[1 - e^{\frac{-\left(\varepsilon - \frac{\sigma_{y}}{k_{1}}\right)k_{2}}{f(\sigma_{u} - \sigma_{y})}} \right] + \sigma_{y}, \ \varepsilon > \varepsilon_{0}.$$
(28)

When ε approaches a large enough value, it gives the following equation:

$$\sigma(\varepsilon)|_{\varepsilon \to \infty^+} = \sigma_{\rm u}. \tag{29}$$

Thus, the stress-strain model of perforated steel blocks can be described as follows:

$$\sigma(\varepsilon) = \begin{cases} k_{1}\varepsilon, & \varepsilon \leq \varepsilon_{0} \\ (\sigma_{u} - \sigma_{y}) \left[(f - 1)e^{\frac{-\left(\varepsilon - \frac{\sigma_{y}}{k_{1}}\right)k_{2}}{f(\sigma_{u} - \sigma_{y})}} + 1 \right] \left[1 \quad \varepsilon > \varepsilon_{0} \\ - e^{\frac{-\left(\varepsilon - \frac{\sigma_{y}}{k_{1}}\right)k_{2}}{f(\sigma_{u} - \sigma_{y})}} \right] + \sigma_{y}, \end{cases}$$

$$(30)$$

where f is a constant parameter that controls the curvature of the curve after the elastic stage, and *f* is suggested to be 0.3 according to Zhou and Wu [27].

5.5 Model verification

The comparisons of stress-strain curves obtained in tests is shown in Figure 24 along with FE simulations and parametric predictions. It should be noted that the shape of stress-strain curves of specimens is shown in Figure 24 match the assumption made in Figure 22, and this kind of stress-strain curve takes the ultimate strength, ductility, and yield strength-to-peak strength ratio into consideration. As can be seen in Figure 24, the stress-strain curve obtained according to parametric models (equation 30) matches well with both the experimental data and FE simulations in terms of the elastic and inelastic stages.

6 Conclusion

In this study, the effects of different key parameters (i.e., hole number per layer n, wedge-shape coefficient ϕ , void ratio r, solid segment length L_0 , and hole arrangement coefficient h) on the stress-strain behavior of perforated steel blocks are experimentally, numerically, and analytically investigated. First, 12 compressive tests were conducted with the purpose to calibrate the FE modeling technique and the proposed stress-strain equations. Then, using the verified FE models, systematic parametric studies were carried out for the perforated steel block, and reasons for the mechanical performance varying with each parameter were given. Finally, a stress-strain model was proposed for the developed CY material. The following conclusions can be drawn:

- (1) Test results show that the ultimate compressive strain of mild steel block is extraordinarily large (within a range from 4.2 to 24%) under well-designed perforations, thus it can be used as CY material.
- (2) Parametric studies based on verified FE models indicated that void ratio (r) and hole arrangement coefficient (h) are the most critical parameters influencing member stiffness, ultimate strength, and yield strengthto-peak strength ratio (λ). Theoretically, the λ value that is close to 1.0 is ideal for CY material. To reach a reasonable λ value, r and h are the key parameters to be considered.
- (3) The test results and FE simulations form a dataset, based on which parametric formulae that can be used to predict the stiffness and the ultimate strength of perforated block under compression are proposed through regression analysis.
- (4) A four-parameter theoretical model was used to develop the stress-strain relationship of perforated steel block, and the proposed models match well with both experimental curves and FE simulations.

It should be noted that the formulae are developed to predict the material response of perforated steel blocks under limited parameter ranges. Further research is needed to verify the model more concretely and extend the application scope (e.g., using another metallic material) before they can be used in practice. The method of perforation, FE modeling technique, and the framework for developing stress-strain models for mild steel can be extended to other metallic materials with certain modifications.

Acknowledgments: The authors gratefully acknowledge the financial support from the National Natural Science Foundation of China (NSFC) (Grants No. 51878414; 52008255), the Ministry of Science and Technology of China (Grant No. 2018YFE0125000), NSFC and Guangdong province (Grants No. U2001226), Natural Science Foundation of Guangdong province (Grant No. 2021A1515010474), and Guangdong Provincial Key Laboratory of Durability for Marine Civil Engineering (Grants No. 2020B1212060074).

Funding information: National Natural Science Foundation of China (NSFC) (Grants No. 51878414; 52008255), the Ministry of Science and Technology of China (Grant No. 2018YFE0125000), NSFC and Guangdong province (Grants No. U2001226), Natural Science Foundation of Guangdong province (Grant No. 2021A1515010474), and Guangdong Provincial Key Laboratory of Durability for Marine Civil Engineering (Grants No. 2020B1212060074).

Author contributions: Yingwu Zhou: conceptualization, funding acquisition, writing - original draft; Li Zhuang: Investigation, formal analysis; Zhiheng Hu: Investigation, Visualization; Biao Hu: Formal analysis, Writing -original draft, Writing - review & editing; Xiaoxu Huang: Resources; Shan li: Validation; Menghuan Guo: Validation; Zhongfeng Zhu: Validation.

Conflict of interest: Authors state no conflict of interest.

References

- [1] Zhou, Y., X. Chen, X. Wang, L. Sui, X. Huang, M. Guo, et al. Seismic performance of large rupture strain FRP retrofitted RC columns with corroded steel reinforcement. *Engineering* Structures, Vol. 216, 2020, id. 110744.
- [2] Hu, B., Y. W. Zhou, F. Xing, L. L. Sui, and M. S. Luo. Experimental and theoretical investigation on the hybrid CFRP-ECC flexural strengthening of RC beams with corroded longitudinal reinforcement. *Engineering Structures*, Vol. 200, 2019, id. 109717.
- [3] Zhang, P., H. S. Zhang, G. Cui, X. D. Yue, J. J. Guo, and D. Hui. Effect of steel fiber on impact resistance and durability of concrete containing nano-SiO₂. Nanotechnology Reviews, Vol. 10, No. 1, 2021, pp. 504–517.

- [4] Tuutti, K. Corrosion of steel in concrete, Swedish Cement and Concrete Research Institute, Stockholm, Sweden, 1982.
- [5] Ou, Y. C., H. D. Fan, and N. D. Nguyen. Long-term seismic performance of reinforced concrete bridges under steel reinforcement corrosion due to chloride attack. *Earthquake Engineering & Structural Dynamics*, Vol. 42, No. 14, 2013, pp. 2113–2127.
- [6] Zhou, Y., M. Guo, L. Sui, F. Xing, B. Hu, Z. Huang, et al. Shear strength components of adjustable hybrid bonded CFRP shearstrengthened RC beams. *Composites Part B*, Vol. 163, 2019, pp. 36–51.
- [7] Zhou, Y., L. Sui, X. Huang, M. Guo, M. Luo, B. Hu, et al. Enhancing the EB-FRP strengthening effectiveness by incorporating a cracking-control layer of ECC with different thicknesses. Construction and Building Materials, Vol. 286, 2021, id. 122975.
- [8] Hu, Z. H., X. Q. Zhou, M. H. Guo, X. X. Huang, and B. Hu. Enhancing the performance of CFRP shear-strengthened RC beams using "ductile" anchoring devices. Frontiers in Materials, Vol. 7, 2020, id. 292.
- [9] Naaman, A. E. FRP reinforcements in structural concrete: assessment, progress and prospects. *Proceedings of the Sixth International Symposium on FRP Reinforcement for Concrete Structures*, World Scientific, Singapore, 2003, pp. 1–24.
- [10] Wu, Y. F. New avenue of achieving ductility for reinforced concrete members. *Journal of Structural Engineering*, Vol. 132, No. 9, 2006, pp. 1502–1506.
- [11] Park, R. Ductility evaluation from laboratory and analytical testing. Proceedings of the 9th World Conference on Earthquake Engineering, Vol. 8, Tokyo-Kyoto, Japan, 1988, 605–616.
- [12] Gao, F., Z. Q. Tang, S. L. Mei, B. Hu, S. T. Huang, and J. B. Chen. Seismic behavior of exterior beam-column joints with high-performance steel rebar: Experimental and numerical investigations. *Advances in Structural Engineering*, Vol. 24, No. 1, 2021, pp. 90–106.
- [13] Gao, F., Z. Q. Tang, B. Hu, J. B. Chen, H. P. Zhu, and J. Ma. Investigation of the interior RC beam-column joints under monotonic antisymmetrical load. *Frontiers of Structural and Civil Engineering*, Vol. 13, 2019, pp. 1474–1494.
- [14] Wu, Y. F. Ductility demand of compression yielding fiber-reinforced polymer-reinforced concrete beams. ACI Structural Journal, Vol. 105, No. 1, 2008, pp. 104–110.
- [15] Wu, Y. F., J. F. Jiang, and K. Liu. Perforated SIFCON blocks An extraordinarily ductile material ideal for use in compression yielding structural systems. *Construction and Building Materials*, Vol. 24, No. 12, 2010, pp. 2454–2465.
- [16] Wu, Y. F., Y. W. Zhou, and X. Q. He. Performance-based design of compression-yielding FRP-reinforced concrete beams. *Composite Structures*, Vol. 93, No. 1, 2010, pp. 113-123.
- [17] Wu, Y. F. and Y. W. Zhou. Controlling the damage of concrete columns through compression yielding. *Structural Control & Health Monitoring*, Vol. 18, No. 8, 2011, pp. 890-907.
- [18] Naaman, A. E. and S. M. Jeong. Structural ductility of beams prestressed with FRP tendons. Proceedings of the 2nd International Symposium on Non-metallic (FRP) Reinforcement for Concrete Structures, RILEM Proceedings 29, L. Taerwe, editor, E & FN Spon, Ghent, Belgium, London, August 1995, pp. 379–386.
- [19] Kośla, K., M. Olejnik, and K. Olszewska. Preparation and properties of composite materials containing graphene

- structures and their applicability in personal protective equipment: a Review. Reviews on Advanced Materials Science, Vol. 59, No. 1, 2020, pp. 215-242.
- [20] Hu, B. and Y. F. Wu. Effect of shear span-to-depth ratio on shear strength components of RC beams. Engineering Structures, Vol. 168, 2018, pp. 770-783.
- [21] Hu, B. and Y. F. Wu. Quantification of shear cracking in reinforced concrete beams. Engineering Structures, Vol. 147, 2017, pp. 666-678.
- [22] Wu, Y. F. and B. Hu. Shear strength components in reinforced concrete members. Journal of Structural Engineering, Vol. 143, No. 9, 2018, id. 04017092.
- [23] ABAQUS. ABAQUS analysis user's manual. Version 6.11, 2011.

- [24] Xiao, Y. X. and T. J. Ma. Research on Finite Element Simulation of Sheet Metal Stamping. Forging & Stamping Technology, Vol. 37, No. 1, 2012, pp. 165-168.
- [25] Han, L. H. Concrete filled steel tubular structures: theory and practice (the third edition), Science Press, Beijing, China, 2016.
- [26] Wu, Y. F., Y. W. Zhou, B. Hu, X. X. Huang, and S. T. Smith. Fused structures for safer and more economical constructions. Frontiers of Structural and Civil Engineering, Vol. 14, No. 1, 2020, pp. 1-9.
- [27] Zhou, Y. W. and Y. F. Wu. General model for constitutive relationships of concrete and its composite structures. Composite Structures, Vol. 94, No. 2, 2012, pp. 580-592.